







Article

Quatsomes Loaded with Squaraine Dye as an Effective Photosensitizer for Photodynamic Therapy

Nicolò Bordignon^{1,2}, Mariana Köber^{1,3} , Giorgia Chinigò², Carlotta Pontremoli⁴, Ettore Sansone², Guillem Vargas-Nadal^{1,3}, Maria Jesus Moran Plata^{4,†} , Alessandra Fiorio Pla² , Nadia Barbero^{4,*} , Judit Morla-Folch^{1,*,‡}  and Nora Ventosa^{1,3,*} 

¹ Institut de Ciència de Materials de Barcelona, ICMAB-CSIC, Campus UAB, Bellaterra, 08193 Catalonia, Spain

² Department of Life Sciences and Systems Biology, University of Torino, Via Accademia Albertina 13, 10123 Turin, Italy

³ CIBER de Bioingeniería, Biomateriales y Nanomedicina, Instituto de Salud Carlos III, 08193 Bellaterra, Spain

⁴ Department of Chemistry, NIS Interdepartmental Centre and INSTM Reference Centre, University of Torino, Via Quarello 15a, 10135 Turin, Italy

* Correspondence: nadia.barbero@unito.it (N.B.); jmorla@icmab.es (J.M.-F.); ventosa@icmab.es (N.V.)

† Present address: Donostia International Physics Center, Paseo Manuel de Lardizabal 4, 20018 Donostia, Spain.

‡ Present address: BioMedical Engineering and Imaging Institute, Icahn School of Medicine at Mount Sinai, New York City, NY 10029, USA.

Abstract: Photodynamic therapy is a non-invasive therapeutic strategy that combines external light with a photosensitizer (PS) to destroy abnormal cells. Despite the great progress in the development of new photosensitizers with improved efficacy, the PS's photosensitivity, high hydrophobicity, and tumor target avidity still represent the main challenges. Herein, newly synthesized brominated squaraine, exhibiting intense absorption in the red/near-infrared region, has been successfully incorporated into Quatsome (QS) nanovesicles at different loadings. The formulations under study have been characterized and interrogated in vitro for cytotoxicity, cellular uptake, and PDT efficiency in a breast cancer cell line. The nanoencapsulation of brominated squaraine into QS overcomes the non-water solubility limitation of the brominated squaraine without compromising its ability to generate ROS rapidly. In addition, PDT effectiveness is maximized due to the highly localized PS loadings in the QS. This strategy allows using a therapeutic squaraine concentration that is 100 times lower than the concentration of free squaraine usually employed in PDT. Taken together, our results reveal the benefits of the incorporation of brominated squaraine into QS to optimize their photoactive properties and support their applicability as photosensitizer agents for PDT.

Keywords: nanovesicles; quatsomes; squaraine; photodynamic therapy



Citation: Bordignon, N.; Köber, M.; Chinigò, G.; Pontremoli, C.; Sansone, E.; Vargas-Nadal, G.; Moran Plata, M.J.; Fiorio Pla, A.; Barbero, N.; Morla-Folch, J.; et al. Quatsomes Loaded with Squaraine Dye as an Effective Photosensitizer for Photodynamic Therapy. *Pharmaceutics* **2023**, *15*, 902. <https://doi.org/10.3390/pharmaceutics15030902>

Academic Editor: Maria Nowakowska

Received: 5 February 2023

Revised: 21 February 2023

Accepted: 23 February 2023

Published: 10 March 2023



Copyright: © 2023 by the authors. Licensee MDPI, Basel, Switzerland. This article is an open access article distributed under the terms and conditions of the Creative Commons Attribution (CC BY) license (<https://creativecommons.org/licenses/by/4.0/>).

1. Introduction

Photodynamic Therapy (PDT) is a minimally invasive localized clinical treatment that has been developed to treat many diseases, including psoriasis [1,2] or several types of cancer [3–5]. PDT is based on the presence of three components: a photosensitizer (PS), light, and molecular oxygen. Studies on cells and animals started in the 1960s and led to the clinical approval by the Food and Drug Administration (FDA) of the first photosensitizer, Photophrin, in 1995 [5,6]. In PDT, PSs are exposed to light at a specific wavelength, depending on the nature of the molecule in use [7]. After irradiation, the PS absorbs the light, causing the electron to transition from its ground state (singlet state) to an excited singlet state. Then, the PS can lose energy and return to the ground state. Alternatively, the singlet state can undergo intersystem crossing (ISC), forming an excited triplet state caused by the spin conversion of the electron in the higher energy orbital. From this triplet state, the molecule can relax and go back to the singlet state via two different routes: (i) the molecule can reduce the substrate forming radicals, which then react with the oxygen,

producing oxygenated radicals (Reactive Oxygen Species, ROS), known as a Type I reaction, or (ii) the PS can directly react with molecular oxygen, producing singlet oxygen ($^1\text{O}_2$), known as a Type II reaction [8,9]. These reactions also explain the importance of oxygen's presence in PDT. Both products then induce apoptosis or necrosis, causing damage to tumor cells and tumor-associated vascular structures, contributing to the stimulation of the immune response in the host [5,10].

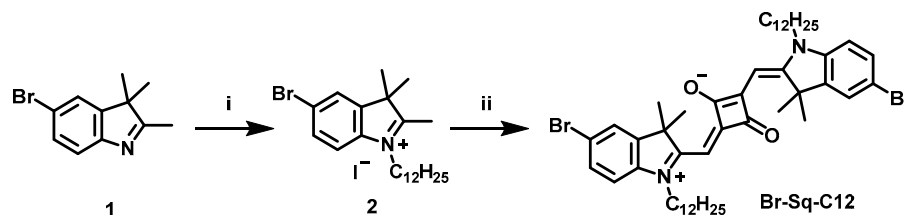
For a safe and effective photodynamic treatment, the PS must be non-cytotoxic in the dark but highly cytotoxic after irradiation, photo- and chemically stable, non-mutagenic, and selective against neoplastic tissues. In addition, it should present a high degree of purity and ideally absorb light between 600 and 800 nm to promote a deeper tissue penetration and minimize light scattering by tissues [11,12]. Most of the FDA-approved or currently under clinical trials PS [13,14] are based on porphyrins or chlorin structures, such as Photofrin [15] or Foscan [16,17], porfimer sodium and temoporfin, respectively. Those PS, based on an extended aromatic ring system, are highly hydrophobic and susceptible to π - π stacking. This results in poor solubility in aqueous media and rapid clearance in blood circulation, severely compromising the therapeutic effectiveness of PDT. In this context, organic dyes, such as polymethine dyes (squaraine and cyanine dyes), represent a promising alternative to PS thanks to the higher selectivity, purity, and absorption at longer wavelengths compared to porphyrin-derived PS [18–22]. Indeed, both cyanine and squaraine dyes have shown excellent light-induced toxicity on different types of tumors.

Despite the many merits of improving PS performances, the poor water solubility (leading to aggregation in aqueous media) and low chemical stability are still the main challenges for their biomedical application [21,23,24]. In order to improve the PSs' performances and to protect them from photodegradation, different delivery systems have been developed [24–27], with liposomes and polymeric micelles being the most common ones. These colloidal nanostructures—formed by the self-assembly of amphiphilic molecules in water—are used for the encapsulation of non-water-soluble PS in either the hydrophobic core of micelles [28] or the membrane of liposomes [29,30]. It is worth noting that other strategies, such as the insertion of functional groups into the PS structure to increase water solubility, have been reported [31]. However, those modifications usually compromise the photochemical properties of the PS [32]. Thus, the nanoencapsulation of the PS improves its solubility in the aqueous environment without altering its chemical structure and benefits from either active targeting, with the functionalization of targeting agents [33–35], or passive targeting through the enhanced permeation and retention effect (EPR) [36]. However, most of those formulations are limited by the lack of stability over time. For example, liposomes tend to change morphology, aggregate, or suffer from PS leakage over time [37,38], thus requiring complex formulations and coatings [39] to overcome these aspects.

To address these challenges, in the present work, we have employed non-liposomal nanovesicles, named quatsomes (QS), as a nanocarrier for a hydrophobic squaraine dye. QS are non-liposomal thermodynamically stable nanometric vesicles with very low dispersity [40] composed of sterols and quaternary ammonium surfactants [41]. These sterols and surfactants self-assemble in water, forming amphiphilic spherical nanometric structures with high homogeneity. This kind of vesicle has been proven to be safe and non-toxic for biomedical applications and has remained stable for years [42,43]. The encapsulation of PSs into QS is an attractive approach since it offers not only a strategy to bring non-soluble squaraine dyes into an aqueous media but also a list of advantages for its *in vivo* application: (i) longer times in circulation and higher cellular uptake [44,45], (ii) improved therapeutic efficiency with a lower dye concentration since the photosensitizer is highly localized at the therapeutic site [42,46] and, (iii) QS allows a targeted delivery by the nanovesicle functionalization with targeting units [47,48].

In previous work, Bromo-Squaraine-C4 (Br-Sq-C4), a newly synthesized squaraine photosensitizer, demonstrated successful results *in vitro* [49]. However, a small organic molecule has important limitations for its *in vivo* application, such as low solubility and poor spectroscopic properties in aqueous media and a tendency to aggregate. Thus, as a

first trial, non-water soluble Br-Sq-C4 was incorporated into QSs nanovesicles to enhance its stability in aqueous media. Nonetheless, Br-Sq-C4 entrapment efficiency was lower than 50% after preparation and not stably anchored into the QS membrane over time, showing significant dye leaking with only 15% of the initial dye concentration remaining after 6 weeks (see Figure S1 in the Supporting Information). Considering the low dye loading efficiency as well as the instability of this system, the use of Br-Sq-C4-loaded QS as a potential photosensitizer agent was dismissed. Instead, we synthesized a similar squaraine bearing longer alkyl chains (**Br-Sq-C12**, see Scheme 1), i.e., C12 instead of C4 hydrocarbon chains. By the incorporation of this longer hydrocarbon chain, **Br-Sq-C12** can be anchored to the QS membrane stably due to its larger lipophilicity.



Scheme 1. Synthesis of **Br-Sq-C12** dye. (i) anhydrous acetonitrile, iodododecane, MW, 60 min, 155 °C; (ii) squaric acid, toluene/n-butanol (1:1), MW, 30 min, 160 °C.

Herein, in this work, we present the design of a new QS composed of Cholesterol and surfactant Sterealkonium Chloride loaded at different concentrations of **Br-Sq-C12** (Figure 1). First, we studied the physicochemical and spectroscopic characteristics of newly synthesized Br-Sq-C12-loaded quatsomes. The entrapment of Br-Sq-C12 into the QSs does not interfere with its ability to generate ROS rapidly, an essential requirement for PDT activity. Cellular uptake and PDT efficiency are then studied in vitro in a cancer cell model showing the benefits of loading Br-Sq-C12 into a QS vs. Br-Sq-C12 in its free form. In addition to overcoming the non-water solubility limitation of Br-Sq-C12, the nanometric volume facilitated by the QS allows highly localized PS loadings, maximizing in this way the PDT effectiveness. This Br-Sq-C12-loaded QS can not only be explored for the development of highly efficient PDT treatment against cancer but also offers a basis to attain the development of photosensitizers with improved characteristics for in vivo applications.

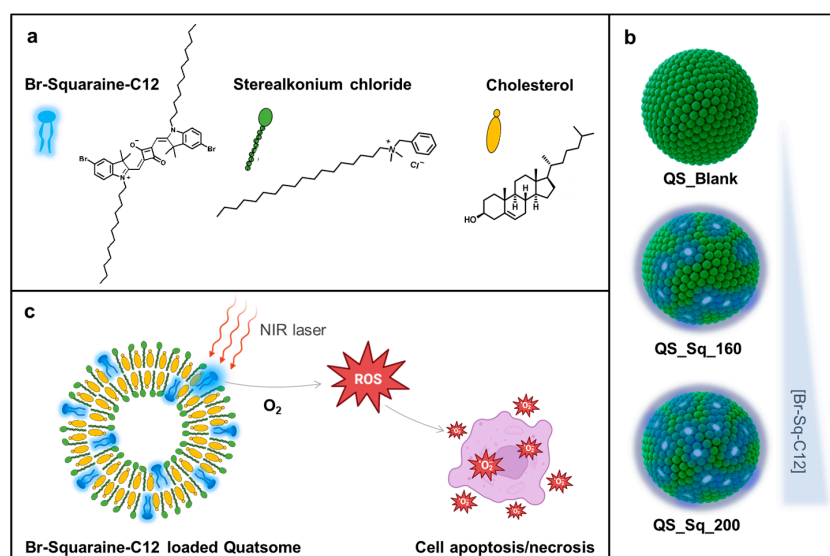


Figure 1. Br-Squaraine-C12-loaded QS components (a); graphic representation of the nanoparticles studied (b); schematic composition of the dye-loaded quatsomes and their mechanism of action in PDT (c).

2. Materials and Methods

2.1. Synthesis of Bromo-Squaraine-C12 Dye

All the chemicals were purchased from Merck (Darmstadt, Germany), Alfa Aesar (Haverhill, MA, USA), or TCI (Tokyo, Japan) and were used without any further purification. All microwave reactions were performed in single-mode Biotage Initiator 2.5 (Biotage, Uppsala, Sweden). TLC was performed on silica gel 60 F254 plates. ^1H NMR (600 MHz) spectra were recorded on a Bruker Avance 600 NMR (Bruker, Billerica, MA, USA) in CDCl_3 . ESI-MS spectra were recorded using an LTQ Orbitrap (Thermo Scientific, Waltham, MA, USA) spectrometer, with an electrospray interface and ion trap as a mass analyzer. The flow injection effluent was delivered into the ion source using nitrogen as sheath and auxiliary gas.

As previously reported, 5-bromo-2,3,3-trimethyl-3H-indole (**1**) was synthesized [50].

2.1.1. Quaternarization Synthesis of Indolenine 5-Bromo-1-dodecyl-2,3,3-trimethyl-3H-indol-1-ium Iodide

All together, 5-bromo-2,3,3-trimethyl-3H-indole (**1**) (500 mg, 2.1 mmol), iodododecane (1.6 mL, 6.3 mmol), and anhydrous acetonitrile (10 mL) were introduced in a reaction vial, sealed with a crimp cap and heated in a microwave system at 155 °C for 60 min. At the end of the reaction, acetonitrile was removed in the rotavapor, and diethyl ether (200 mL) was then poured to precipitate a white-brownish solid, which was washed three times with diethyl ether and filtered (287 mg, 25.5% yield).

^1H NMR (600 MHz, CDCl_3): δ 7.78 (dd, $J = 8.6, 1.8$ Hz, 1H), 7.73 (d, $J = 1.8$ Hz, 1H), 7.57 (d, $J = 8.6$ Hz, 1H), 4.65 (t, 2H), 2.99 (s, 3H), 1.68 (s, 6H), 1.24 (m, 20H), 0.87 (t, $J = 7.0$ Hz, 3H).

^{13}C NMR: The compound solubility proved too low to record a ^{13}C NMR spectrum.

2.1.2. Synthesis of Br-Sq-C12

Compound **2** (287 mg, 0.54 mmol), 4-dihydroxycyclobut-3-ene-1,2-dione (30.8 mg, 0.27 mmol), and 5 mL of a mixture of toluene and n-butanol (1:1) were introduced inside a sealed MW vial and heated up to 160 °C for 30 min. The solution turned blue, and the TLC (Pet. Ether: Acetone 8:2) showed reaction completion. After solvent evaporation, column chromatography (Pet. Ether: Acetone 70:30) afforded **Br-Sq-C12** as a golden solid (140 mg, yield = 60%). ^1H NMR and ESI-MS spectra are shown in Figures S2 and S3, respectively.

^1H NMR (600 MHz, CDCl_3): δ 7.44 (s, 2H), 7.41 (d, $J = 8.3$ Hz, 2H), 6.83 (d, $J = 8.3$ Hz, 2H), 5.94 (s, 2H), 3.92 (s, 4H), 1.77 (s, 12H), 1.24 (m, 40H), 0.87 (t, $J = 6.9$ Hz, 6H).

^{13}C NMR: The compound solubility proved too low to record a ^{13}C NMR spectrum.

HRMS (ESI) m/z : $[\text{M}]^+$ calcd for $[\text{C}_{50}\text{H}_{71}\text{Br}_2\text{N}_2\text{O}_2]^+$ 889.3877, found 891.3869.

2.2. Preparation of Dye-Loaded Chol/Stk QS by DELOS-Susp

All the QS formulations described were prepared using the DELOS-susp method [47,51]. The employed quantities (Table S1) and the detailed protocol used are listed in the Supporting Information. To prepare the organic phase of the DELOS-susp, the desired amount of Chol (PanReac AppliChem, Castellar del Vallès, Spain) and Stk (TokyoChemical Industry CO. LTD, Tokyo, Japan) was dissolved in ethanol (HPLC grade purity, Avantor Performance Materials Poland S.A., Silesia, Poland). This ethanolic solution contains the already solubilized **Br-Sq-C12** (see Table 1 for the exact concentration of each component). The solution was introduced in the high-pressure vessel, and the compressed CO_2 was added, with a final temperature of 38 °C and 11.5 MPa of pressure. After one hour, the expanded solution with all the membrane components dissolved was depressurized over the desired amount of water. After the production, the dye-loaded Chol/Stk QS was purified using diafiltration to remove ethanol and the non-incorporated dye and membrane components.

Table 1. Initial concentrations (pre-processing) used for preparing the nanovesicles.

Nanovesicle Sample	(Br-Sq-C12) (μM)	(Membrane Components) (mg/mL)
QS_Blank	/	5.88
QS_Sq_160	200	5.88
QS_Sq_200	300	5.88

Determination of the Dye Concentration and Dye Loading in QS Nanovesicles

The concentration of dye entrapped in QS was determined by measuring the UV-Vis absorbance A using a UV-Vis spectrophotometer (V-780, Jasco, Easton, Sweden) and a high precision cell (Hellma Analytics, Müllheim, Germany) with a pathlength l of 1 cm. All the samples were diluted in ethanol to disrupt the membrane and release all the entrapped dye molecules. The concentration C of **Br-Sq-C12** was determined using the Lambert-Beer law ($A = \epsilon l C$), knowing that the extinction coefficient (ϵ) of **Br-Sq-C12** in EtOH is $290.484 \text{ M}^{-1} \text{ cm}^{-1}$.

The dye-loading coefficient was determined by lyophilization of the samples (LyoQuest-80, Telstar, Terrassa, Spain) at 193 K and 5 Pa for 5 days. Then, the samples were weighted, and the loading in mass was determined through the following equation.

$$\text{dye loading} = \frac{\text{mass of dye}}{\text{mass of all vesicle components} - \text{mass of dye}}$$

2.3. Spectroscopic Characterization of Free Br-Sq-C12 and Dye-Loaded Qs

2.3.1. UV-Vis Spectroscopy, Molar Extinction Coefficient, and Solvatochromism

To determine the molar extinction coefficient of the **Br-Sq-C12**, different dilutions in ethanol were prepared from a stock solution (0.5 mM). The absorbances were measured and their maxima were plotted vs. the sample concentration, being the slope of the linear fitting of the molar extinction coefficient (ϵ). The analysis was performed in duplicate and data were considered acceptable when the difference between the measured $\log \epsilon$ was equal to or lower than 0.02 to their average.

The determination of the solvatochromism was performed by preparing different solutions of **Br-Sq-C12** and dye-loaded Qs in acetone, absolute ethanol (EtOH), methanol (MeOH), double distilled water (ddH₂O), and Dimethyl sulfoxide (DMSO). The absorption was measured at room temperature by UV-Vis spectroscopy (Cary 300 Bio spectrophotometer, Varian, Santa Clara, USA or V-780, Jasco, Easton, Sweden) in the range of 500–800 nm using quartz cuvettes, using a 1 cm path length.

2.3.2. Fluorescence Spectroscopy

Fluorescence emission measurements were acquired in steady-state mode and recorded in the range of 595–750 nm using a Horiba Jobin Yvon Fluorolog 3 TCSPC fluorimeter (Kyoto, Japan) equipped with a 450-W Xenon lamp and a Hamamatsu R928 photomultiplier (Hamamatsu photonics, Hamamatsu, Japan) by using solvents with different polarity to investigate the solvatochromic behavior of both the **Br-Sq-C12** and dye-loaded QS. The excitation wavelength was different depending on the solvents and was set at the squaraine hypochromic shoulder previously recorded at the UV-Vis spectra. The excitation and emission slits were 5 nm and 5 nm, respectively.

Fluorescence quantum yields (QY) were determined using the same instrument with Quanta- ϕ integrating sphere and De Mello method. The QY was evaluated in absolute ethanol for the **Br-Sq-C12** and ddH₂O for the dye-loaded Qs. The analyzed samples had an absorbance of around 0.1 to avoid aggregations/fluorescence quenching. The final result is an average of three independent measurements of different dye solutions.

Fluorescence lifetimes (LT) were determined using the time-correlated single photon counting method (Horiba Jobin Yvon, Horiba, Kyoto, Japan) using a 636 nm Horiba Jobin Yvon NanoLED (Horiba, Kyoto, Japan) as the excitation source and a pulse repetition

frequency of 1 MHz positioned at 90° with respect to a TBX-04 detector. Lifetimes were calculated using DAS6 decay analysis software. The LT was evaluated in absolute ethanol for the **Br-Sq-C12** and ddH₂O for the dye-loaded QSs.

2.4. Physicochemical Characterization and Stability of Dye-Loaded QS

2.4.1. Dynamic Light Scattering (DLS) and Electrophoretic Light Scattering (ELS)

The mean size and size distribution of the QS loaded with 200 and 300 µM **Br-Sq-C12** (QS_Sq_160 and QS_Sq_200, respectively) were determined by DLS, while the determination of the ζ-potential values (z-pot) was performed with the ELS. Both measurements were carried out using a Zetasizer Ultra (Malvern Instruments, Malvern, UK). The measurements with the DLS technique were performed using a fluorescence filter to block the light resulting from fluorescence emission, which may alter the correlation function (the instrument exploits a 633 nm laser). Meanwhile, the ELS measurements were performed employing a DTS1070 folded capillary cell (Malvern Instruments, Malvern, UK) was used, applying a voltage of 40 mV between the gold electrodes, and being calculated using the Helmholtz–Smoluchowski equation, which can potentially underestimate the real zeta-potential [52,53]. All the measurements were performed in triplicate to ensure the reliability of the results.

2.4.2. Cryogenic Transmission Electron Microscopy

Cryogenic transmission electron microscopy (cryo-TEM) images were acquired with a JEOL JEM microscope (JEOL JEM 2011, Tokyo, Japan) operating at 200 kV under low-dose conditions. First, 10 µL of the sample was deposited onto the holey carbon grid and, immediately after, vitrified by rapid immersion in liquid ethane. The vitrified sample was mounted on a cryo-transfer system and introduced into the microscope (Gatan 626, Gatan, Pleasanton, CA, USA). Images were recorded on a CCD camera (Gatan Ultrascan US1000, Gatan, Pleasanton, CA, USA).

2.5. Evaluation of ROS Generation with DPBF and DCFH

As a probe molecule, 1,3-Diphenylisobenzofuran (DPBF, Sigma Aldrich, Darmstadt, Germany) was used to evaluate Reactive Oxygen Species (ROS) generation by following the protocol previously described in the literature [49]. DPBF rapidly reacts with ¹O₂ forming the colorless *o*-dibenzoylbenzene derivative. The ¹O₂ scavenger activity can be monitored through a decrease in the electronic absorption band of DPBF at 415 nm. Stock solutions were prepared in DMSO, absolute ethanol, and phosphate buffer (2 mM, pH 7.4), respectively, for DPBF, free **Br-Sq-C12**, and **Br-Sq-C12**-loaded quatsomes. Each solution was then diluted in phosphate buffer (2 mM, pH 7.4) to obtain a DPBF concentration of 25 µM and a final concentration of 2.5 µM for both the free and the encapsulated dye. The solutions were placed in a 1 cm quartz cell and irradiated at various time intervals under stirring in an aerated solarbox (Solarbox 3000e, 250 W xenon lamp, CO.FO.ME.GRA, Milan, Italy). The light was filtered in an optical filter with a 515 nm cut-off to avoid DPBF degradation. At predefined time points (30, 60, 90, 120, and 180 s), absorption spectra were recorded on a Cary 300 Bio spectrophotometer instrument (Varian, Santa Clara, CA, USA). The decrease in the DPBF absorption contribution at 415 nm was plotted as a function of the irradiation time.

2.6. Biological Assays

2.6.1. Cell Culture, Cell Viability, and Phototoxicity Assay

Human breast adenocarcinoma cell line (MCF-7, ECACC, European Collection of Authenticated Cell Cultures, Porton Down, UK) was cultured in DMEM High Glucose (Euroclone, Pero, Italy) growth medium complemented with 10% Fetal Bovine Serum (Euroclone, Pero, Italy), 100 mg/mL PenStrep (Sigma-Aldrich, Saint Louis, MO, USA), and 2 mM L-glutamine (Sigma-Aldrich, Saint Louis, MO, USA). Cells were cultured in a

humidified incubator (HeraCell 150, Heraeus, Hanau, Germany) with 5% CO₂ at 37 °C, using Falcon™ plates as supports.

To investigate QS's cytotoxicity, MCF-7 cells (0.5·10⁴ cells/well) were seeded in 96-well plates (Sarstedt, Nümbrecht, Germany). Six hours after plating, cells were treated with QS_Blank at two different membrane components' (Chol + Stk) final concentrations (10 µg/mL and 2 µg/mL). Cell viability was assessed using CellTiter 96® Aqueous Non-Radioactive cell proliferation assay (Promega, Madison, WI, USA) according to the manufacturer's instructions 24, 48, and 72 h after treatment. Briefly, 2 h after MTS incubation at 37 °C, absorbance at 490 nm was recorded using a microplate reader (FilterMax F5, Multi-Mode Microplate Reader, Molecular Devices, San Jose, MO, USA). Absorbance values were normalized on the control at 24 h and analyzed as being proportional to the number of viable cells. Similarly, the cytotoxicity of QS (2 µg/mL) loaded with increasing dye concentrations (Table 2) was assessed.

Table 2. Concentrations, exposure times, and dilution rates used in PDT tests.

	Br-Sq-C12	QS_Blank (2 µg/mL Membrane Components)	QS_Sq_200 (2 µg/mL Membrane Components)
Dye concentration (nM)	85	0	85
Exposure time (min)	15	15	15
Dilution rate	-	1:2397	1:2130

To evaluate the photodynamic effect of QS_Sq, MCF-7 cells (0.5·10⁴ cells/well) were seeded in 96-well plates. Six hours after plating, cells were treated with QS_Sq at the concentrations reported in Table 2 and Br-Sq-C12 in its free form at the same concentrations. After O/N incubation at 37 °C and 5% CO₂, the cells were irradiated for 15 min with a RED-LED array (96 LEDs in a 12 × 8 arrangement, excitation wavelength: 640 nm, and irradiance: 8 mW/cm²) specifically designed and produced by Cicci Research s.r.l (Grosseto, Italy). Cell viability was assessed 24, 48, and 72 h after irradiation using CellTiter 96® Aqueous Non-Radioactive cell proliferation assay (Promega, Madison, WI, USA) as described above. The photodynamic effect of Br-Sq-C12-loaded QS was evaluated by comparing the viability of cells treated with QS_Sq or with the same concentration of Br-Sq-C12 in its free form upon irradiation. For each condition, eight technical replicates were set up and three independent experiments were performed.

2.6.2. Cellular Uptake

To verify the intracellular uptake of Sq-loaded QS and compare it with that of the dye in its free form, Calcein (Molecular probes®, Invitrogen, Waltham, MA, USA) has been used to label and track the whole cellular volume in MCF-7 live cells. Briefly, MCF-7 cells were seeded in Ibidi µ-Slide 8 wells (1.6 × 10⁴ cells/well), and 24 h after seeding, cells were treated overnight with 85 nM of Br-Sq-C12 in its free form or incorporated within 2 µg/mL QS (QS_Sq_200). After the incubation with the QS_Sq_200, the cells were washed twice with PBS and incubated with Calcein (500 nM) for 30 min, washed twice with Hanks' Balanced Salt Solution (HBSS), and fixed in 4% paraformaldehyde (PAF) at 37 °C for 2 min. The cells were observed using a Leica TCS SP8 confocal system (Leica Microsystems, Wetzlar, Germany) equipped with an HCX PL APO 63X/1.4 NA oil-immersion objective. To simultaneously detect the probes, Br-Sq-C12 was excited with a HeNe laser at 633 nm, whereas Calcein was excited with a DPSS laser at 561 nm. Images were acquired on the three coordinates of the space (XYZ planes) with a resolution of 0.081 µm × 0.081 µm × 0.299 µm and were processed and analyzed with ImageJ software (Rasband, W.S., U.S. National Institutes of Health, Bethesda, MA, USA). Three-dimensional images with Calcein allowed for assessing whether the Br-Sq-C12 encapsulated into QS or in its free form was included within the cellular volume or not.

2.6.3. Statistical Analysis

Data are shown as the average values of three independent pulled experiments \pm standard error mean (SEM). Statistical analyses were performed using Graph-Pad Prism 6.0 software (La Jolla, CA, USA). The statistical significance between different conditions was determined by performing a *t*-test or Mann–Whitney test, according to the populations' distribution (normal or not-normal, respectively). Differences with *p*-values < 0.05 were considered statistically significant and *: *p*-value < 0.05 , ***: *p*-value < 0.0005 , ****: *p*-value < 0.0001 .

3. Results and Discussion

In a previous study, Bromo-Squaraine-C4 (Br-Sq-C4), a non-water soluble indolenine-based dye quaternarized with a four-carbon atom chain, demonstrated successful PDT results in vitro [18,49]. However, Br-Sq-C4 application in biomedicine is hindered by its poor solubility and low chemical stability, especially in aqueous solutions. To overcome this drawback, a promising approach is represented by the incorporation into nanoparticle systems to shield its hydrophobicity, prevent the formation of dye aggregates, and improve solubility in physiological conditions [24,26]. Quatsomes (QS) nanovesicles have shown successful results incorporating different cyanine dyes [42,54–57], demonstrating long-term stability and biocompatibility. Thus, as a first trial, we prepared Br-Sq-C4-loaded quatsomes (QS). However, the incorporation of Br-Sq-C4 into QS resulted in a limited amount of encapsulated dye (entrapment efficiency was $\sim 50\%$), as well as significant dye leaking over time (nearly 50% of Br-Sq-C4 was released after one month, see Figure S1). Considering the low stability of this system, Br-Sq-C4 was dismissed, and a new squaraine bearing a longer alkyl chain, i.e., **Br-Sq-C12**, was developed. By the incorporation of the longer alkyl chain, higher hydrophobicity is provided, hypothesizing that this would promote its stable incorporation in the vesicular membranes. This study evidences the importance of the hydrocarbon chain length for the stabilization of the dye in a vesicular membrane, and in particular, into a quatsome nanovesicle.

3.1. Synthesis of Br-Sq-C12 and Preparation of Br-Sq-C12-Loaded Quatsomes

The synthesis of Bromo-Squaraine-C12, **Br-Sq-C12** dye (Scheme 1 and Figure 1), started with the quaternarization of the bromoindolenine ring (**1**), synthesized following a procedure reported in ref. [49], to obtain compound **2**. This reaction was performed under microwave irradiation and led to increased acidity of the methyl group promoting the following condensation reaction. The final dye was then obtained in a one-step reaction under microwave heating following our well-established method for indolenine-based squaraines [50].

QS composed of Stearalkonium (Stk) and Cholesterol (Chol), with a 1:1 molar ratio Stk/Chol, and loaded with **Br-Sq-C12** were prepared using the DELOS-susp methodology [47] at two different starting concentrations of **Br-Sq-C12**; 200 and 300 μM as initial, pre-processing dye concentration. As a result, two batches of QS encapsulating **Br-Sq-C12** were obtained, named based on their final post-processing dye concentration: QS_Sq_160 and QS_Sq_200, from the 200 and 300 μM , respectively (Figure 2). In addition, non-loaded QS (QS_Blank) was also prepared for comparison with the PS-loaded QS. All formulations were diafiltrated to remove the ethanol and non-entrapped dye or free membrane components from the solution, finally obtaining three batches of water-suspended filtered nanovesicles (see Section 2 for details).

All formulations showed a very similar concentration of membrane components (Table 3). Sample QS_Sq_160 showed a higher average dye encapsulation efficiency ($\sim 80\%$), yielding a final dye concentration of 160 μM , while sample QS_Sq_200 showed, as expected, a higher dye loading in mass (*L*), with an effective dye concentration of $\sim 200 \mu\text{M}$ at the vesicles.

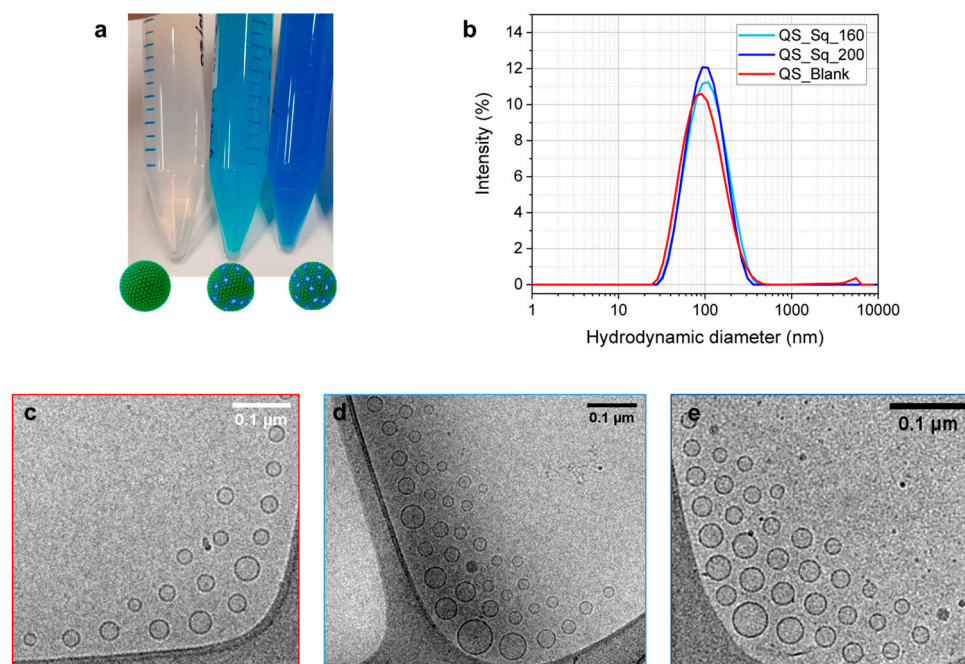


Figure 2. Physicochemical characterization of Br-Sq-C12-loaded quatsomes. Macroscopic appearance of quatsomes after preparation, from left to right; QS_Blank, QS_Sq_160, and QS_Sq_200 (a). Size distribution obtained by DLS (b) and Cryo-TEM images of QS_Blank (c), QS_Sq_160 (d), and QS_Sq_200 (e).

Table 3. Characteristics of the QS_Sq_160 and QS_Sq_200 nanovesicles.

	QS_Blank	QS_Sq_160	QS_Sq_200
(Br-Sq-C12) (μM) ¹	/	159	200
(Membrane components) (mg/mL) ²	4.8	4.4	4.3
Br-Sq-C12 loading in mass ((w/w)%) ³	/	3.20	4.19
d_{hyd} (nm) ⁴	85 \pm 1	92 \pm 1	89 \pm 1
PDI ⁴	0.23 \pm 0.05	0.19 \pm 0.01	0.17 \pm 0.01
ζ -potential (mV) ⁵	92 \pm 3	67 \pm 2	75 \pm 2
Avg. geometric diameter (nm) ⁶	63 \pm 19	66 \pm 20	58 \pm 18

¹ Determined using UV-Vis spectroscopy; ² Determined from the weight of lyophilized; ³ Calculated as mg dye per mg of membrane components (Stk + Chol), $\times 10^{-2}$; ⁴ Average value determined from DLS \pm SD of three repeat measurements; ⁵ Average ζ -potential determined from ELS \pm SD of three repeat measurements; ⁶ Geometric diameter distribution determined from cryo-TEM analysis of one batch \pm SD of the size distribution ($n = 100$).

3.2. Physicochemical Properties

QS_Sq_160 and QS_Sq_200 were analyzed with DLS to determine the mean hydrodynamic diameter and polydispersity index (PDI). First, a systematic DLS study was performed in order to elucidate the optimal dilution for QS measurements. As detailed in the section “Systematic DLS study” included at the SI, DLS, and ELS measurements were performed at 1:10 dilution from the final formulation to ensure reliable results. Average hydrodynamic diameter (z-average), PDI, and ζ -potential average values are summarized in Table 3. Both samples showed similar hydrodynamic diameters (~ 90 nm) and PDI values (< 0.2), with a monomodal size distribution (Figure 2b). In addition, plain quatsomes (QS_Blank) display similar characteristics, confirming the high reproducibility of the QS preparation. A highly positive ζ -potential (~ 70 mV), due to the positive charge of Stearalkonium Chloride, is also comparable among the samples and contributes to the colloidal stability of the nanovesicles [58]. Transmission electron microscopy in cryogenic

conditions (cryo-TEM) confirmed the unilamellar vesicle morphology unaffected by the dye encapsulation (Figure 2c–e). Br-Sq-C12-loaded samples showed high homogeneity in the size distribution (Figure 2d,e), as already shown by the low PDI values obtained in DLS. From the analysis of the cryo-TEM images, the average geometric diameter values were estimated as 66 ± 20 nm and 58 ± 18 nm for QS_Sq_160 and QS_Sq_200, respectively ($n = 100$). It is important to keep in mind that the averaged values obtained from cryo-TEM come from representative images, which help to confirm the data obtained from DLS being this last one more statistically representative.

3.3. Spectroscopic Characterization

Br-Sq-C12 shows an absorption maximum at around 640 nm in ethanol (Figure 3a) with a very high molar extinction coefficient ($290,000 \text{ M}^{-1}\text{cm}^{-1}$). The UV–Vis spectrum is characterized by a narrow absorption band in the NIR, an essential requirement for the PDT treatment, and a characteristic hypsochromic shoulder typical for polymethine dyes. The main absorption peak is associated with the $\pi \rightarrow \pi^*$ HOMO–LUMO transitions, mainly localized on the squaraine core; on the other hand, the shoulder at higher energy can be ascribed to the HOMO–LUMO+1 transition [59,60]. As already observed for other SQs [61], **Br-Sq-C12** shows an excellent fluorescence emission with a maximum emission at 649 nm when dissolved in ethanol, although both the absorption and the fluorescence emission are completely quenched when dissolved in water due to an aggregation caused quenching (ACQ) effect. As shown in Figure 3b,c, the loading into QSs fully overcomes this drawback, increasing the solubility of the dye in aqueous media, with absorbance and fluorescence emission maxima at 644 nm and 655 nm, respectively. The different intensity of the 600 nm shoulder for the free dye in ethanol and the dye-loaded QS is related to the presence of some H-aggregates. However, after the entrapment, the squaraine results are dispersible in 100% water.

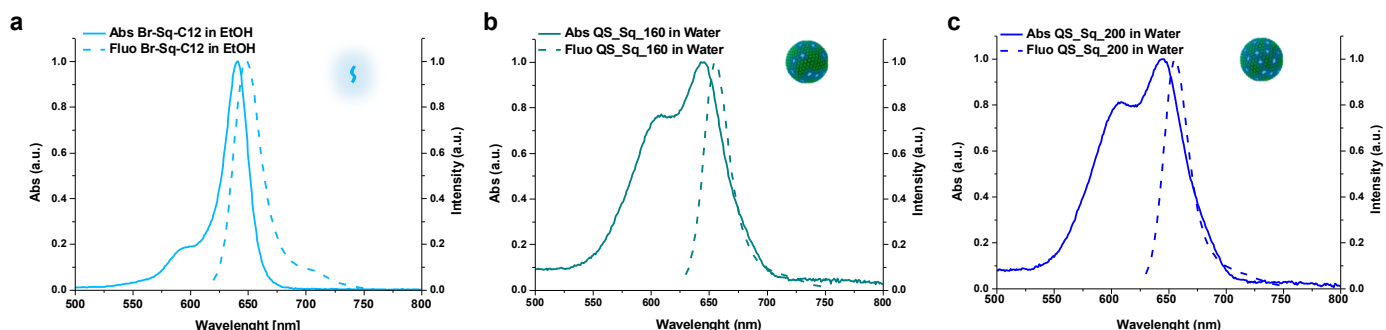


Figure 3. Absorbance and fluorescence emission spectra of free **Br-Sq-C12** in ethanol (a) and **Br-Sq-C12**-loaded QSs in water with a final dye concentration of 160 μM in sample QS_Sq_160 (b) and 200 μM in sample QS_Sq_200 (c).

The solvatochromic effect on both the dye and dye-loaded QSs absorption and emission spectra were also investigated and reported in Table 4. In general, neither the absorption maxima nor the band shape has been affected by the solvent polarity. A slight difference has been observed in the absorption peak maxima in protic or aprotic solvents; in fact, DMSO induced a 15 nm bathochromic shift in comparison to MeOH, suggesting a higher polarity of the ground state compared to the excited state [62–64]. It is worth noticing that both the absorbance and emission maxima of the dye-loaded QSs, irrespective of the amount of incorporated dye, are very close to the values obtained with the free **Br-Sq-C12**, suggesting that the association with the QS did not change the energies and relative probabilities of the electronic transitions. The fluorescence quantum yield of **Br-Sq-C12** in ethanol is in the ranges typical for squaraines in organic media. On the contrary, the QY in water cannot be detected due to the complete insolubility of the dye in aqueous media. However, after the entrapment in the QS, we were able to measure the QY in aqueous dispersion. The values are nevertheless very low, probably due to

the presence of some H-aggregates, as also evidenced in the UV–Vis spectra reported in Figure 3b,c. The **Br-Sq-C12** fluorescence lifetime showed a monoexponentially decay and is in the nanoseconds range, as already observed for several squaraines [59].

Table 4. Photochemical properties of the **Br-Sq-C12** and **Br-Sq-C12**-loaded quatsomes.

	Br-Sq-C12	QS_Sq_160	QS_Sq_200
ϵ ($\times 10^5 \text{ M}^{-1} \text{ cm}^{-1}$)	2.9 ⁽³⁾		
$\lambda_{\text{ex max}}$ (nm)	Not soluble ⁽¹⁾ , 643 ⁽²⁾ , 640 ⁽³⁾ , 638 ⁽⁴⁾ , 650 ⁽⁵⁾	644 ⁽¹⁾ , 643 ⁽²⁾ , 640 ⁽³⁾ , 637 ⁽⁴⁾ , 652 ⁽⁵⁾	644 ⁽¹⁾ , 643 ⁽²⁾ , 640 ⁽³⁾ , 637 ⁽⁴⁾ , 652 ⁽⁵⁾
$\lambda_{\text{em max}}$ (nm)	Not soluble ⁽¹⁾ , 651 ⁽²⁾ , 649 ⁽³⁾ , 645 ⁽⁴⁾ , 660 ⁽⁵⁾	655 ⁽¹⁾ , 653 ⁽²⁾ , 649 ⁽³⁾ , 647 ⁽⁴⁾ , 662 ⁽⁵⁾	655 ⁽¹⁾ , 653 ⁽²⁾ , 649 ⁽³⁾ , 647 ⁽⁴⁾ , 662 ⁽⁵⁾
QY (%)	26 ⁽³⁾	3 ⁽¹⁾	2 ⁽¹⁾
τ (ns)	1.1 (100%) ⁽³⁾	$\tau_1 = 1.4$ (11%) ⁽¹⁾ $\tau_2 = 2.7$ (89%) ⁽¹⁾	$\tau_1 = 1.9$ (16%) ⁽¹⁾ $\tau_2 = 2.9$ (84%) ⁽¹⁾
χ^2	1.03 ⁽³⁾	1.02 ⁽¹⁾	1.00 ⁽¹⁾

⁽¹⁾ Water; ⁽²⁾ Acetone; ⁽³⁾ Ethanol; ⁽⁴⁾ Methanol; ⁽⁵⁾ DMSO.

By comparing the values obtained for QS_Sq_160 and QS_Sq_200 in water, bi-functional equations were necessary to fit the decay curves, suggesting that two different types of interactions occurred with the Qs. Specifically, one fluorescence lifetime is slightly longer, while the other ones (ca. 85%) increased by ca. 2.7 times compared to the free dye. This longer decay could be ascribed to the decrease in rotational/twisting degrees of freedom, confirming a good degree of dye entrapment into the QS vesicles. On the other hand, the shorter lifetime could be due to the presence of a small amount of free dye on the QS surface, leading to a detrimental effect caused by the interaction with highly polar media, such as water [59]. From that data, we can conclude that **Br-Sq-C12** has been successfully incorporated into the QS membrane, allowing its fluorescence in an aqueous media.

3.4. Evaluation of Colloidal Stability and Photostability

Previous works on QS have already demonstrated the long colloidal stability, up to a year, of these nanovesicles [41–43]. In this work, we have evaluated the stability over time and photostability of the **Br-Sq-C12**-loaded QS with DLS and fluorescence spectroscopy, respectively. The obtained data proved the dye-loaded nanovesicular systems to be very stable for 18 months, with hydrodynamic diameter values around 90 nm and optimally low PDI values maintained around 0.2 (Figures 4a and S4). As previously mentioned, the high positive ζ -potential plays a crucial role in providing colloidal stability; thus, +70 mV ζ -potential values after 10 weeks for both dye-loaded systems demonstrated the long-term stability of those nanovesicles (Figure 4b).

Similarly, photostability was evaluated with periodical UV–vis absorbance measurements for up to 18 months. We noticed a lowering of the main absorbance peak at 644 nm during the time for both samples in the study (Figures 4c,d and S5), indicating a decrement in the PS concentration at the QS nanovesicle. The residual dye concentration encapsulated in QS was quantified again 4 months after the production, and the obtained values were $\sim 130 \mu\text{M}$ for sample QS_Sq_160 and $\sim 180 \mu\text{M}$ for sample QS_Sq_200, resulting in a percentual dye leaking of $\sim 20\%$ and $\sim 9\%$ in 4 months, respectively (Figure 4e). In order to better understand this phenomenon, we followed the variation of the peaks' amplitude over time (ratio $\text{peak}_{660\text{nm}}/\text{shoulder}_{600\text{nm}}$), which can be indicative of the formation of dye aggregates. The results, presented in Figure S5, show that both bands progressively decrease over time with no significant change in the ratio, suggesting that there is no significant dye aggregation in the QS membrane. Given the obtained results, we can assume that the stability of the dyes is not compromised in a major way by their inclusion in the QS membrane at the obtained loadings.

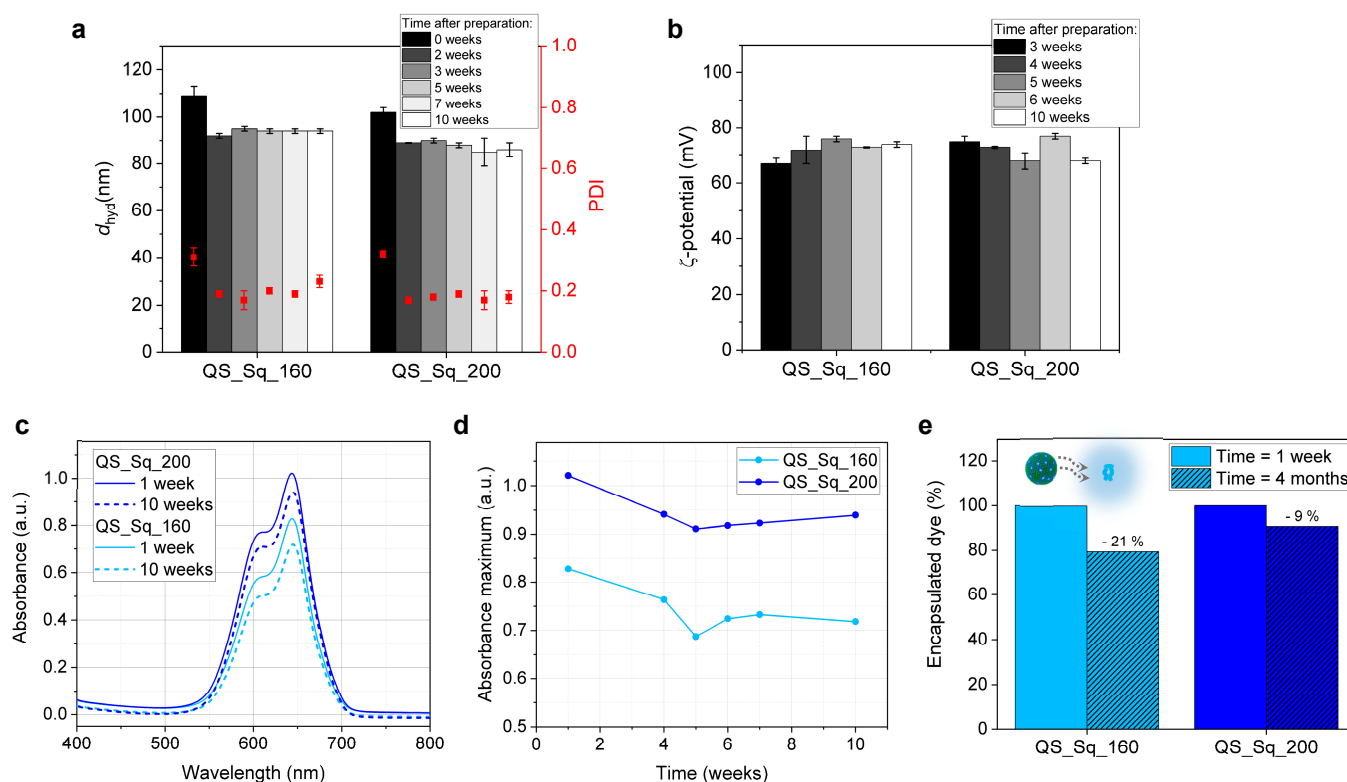


Figure 4. DLS and ELS bar plot, showing hydrodynamic diameters (z-average) as bars and PDI as dots (a) and ζ -potential values (b). Absorbance spectra (c) and maximum absorbance values over time (d), measured at 1:10 dilution. Quantification of dye leaking 4 months after sample preparation (e).

3.5. ROS Production

A preliminary evaluation of the ability of both the free **Br-Sq-C12** and dye-loaded QS to generate Reactive Oxygen Species (ROS) was carried out by using 1,3-diphenylisobenzofuran (DPBF) as a probe [49]. DPBF rapidly reacts with ROS generated by the light-activated dye, resulting in the disappearance of DPBF's characteristic absorption band at 415 nm due to the formation of the colorless o-dibenzoylbenzene derivative. As a function of the irradiation time, the decrease in the DPBF absorption band at 415 nm has been compared to the values obtained by irradiating a standard, the efficient and well-known ROS generator Rose Bengal (RB). As shown in Figure 5, both the free squaraine and the squaraine loaded into Qs possess faster and higher ROS generation ability compared to the RB. In particular, **Br-Sq-C12** is able to promote the complete decay of DPBF absorption within 180 s, while the same result was obtained in 10 min for reference RB. This fast ROS generation could be ascribed to the presence of bromine, which may facilitate the singlet to triplet state intersystem crossing due to the well-known heavy atom effect [18,19]. More importantly, the entrapment of **Br-Sq-C12** into the Qs does not interfere with the ability of the dye to generate ROS rapidly, an essential requirement for PDT activity.

3.6. Cytotoxicity and PDT Assays

Despite the outstanding properties of QS, the remarkable cytotoxicity of quaternary ammonium surfactants, including Stk, could represent a challenge in their *in vivo* application [65,66]. Therefore, to assess QS biocompatibility, we first performed cell viability assays on MCF-7 cells treated with two different concentrations of blank QS, i.e., 10 and 2 $\mu\text{g}/\text{mL}$ (Stk/Chol); see Section 2.6.1 for details. As shown in Figure 6a, QS diluted to a final membrane components' concentration of 10 $\mu\text{g}/\text{mL}$ revealed marked cytotoxicity starting 24 h after treatment and occurring up to 72 h. On the contrary, QS at 2 $\mu\text{g}/\text{mL}$ showed good biocompatibility on MCF-7 cells (Figure 6b). QS_Sq_160 and QS_Sq_200 were diluted to 2 $\mu\text{g}/\text{mL}$ membrane components, corresponding to a final dye concentration

of 68 nM and 85 nM, respectively. Interestingly, the newly synthesized **Br-Sq-C12**-85nM-loaded quatsomes (QS_Sq_200) are slightly more cytotoxic than QS_Blank at 24 and 48 h after treatment with 2 $\mu\text{g}/\text{mL}$, although still highly biocompatible compared to QS_Blank at 10 $\mu\text{g}/\text{mL}$ (Figure 6c). This effect is in agreement with previously reported data on polymethine dyes loaded in solid lipid nanoparticles [24]. Consequently, the measurement of the photoactivity of **Br-Sq-C12**-loaded QS was performed by diluting the formulation up to a membrane components' concentration of 2 $\mu\text{g}/\text{mL}$ to avoid any non-targeted cytotoxicity provided by the carrier itself.

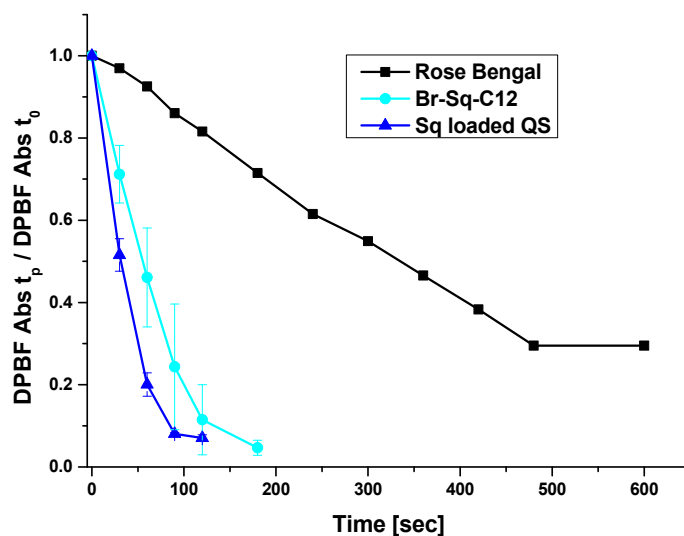


Figure 5. Comparative generation of Reactive Oxygen Species (ROS) using Rose Bengal as the standard reference. The final concentration of the squaraine is 2.5 μM for both free and dye-loaded QS.

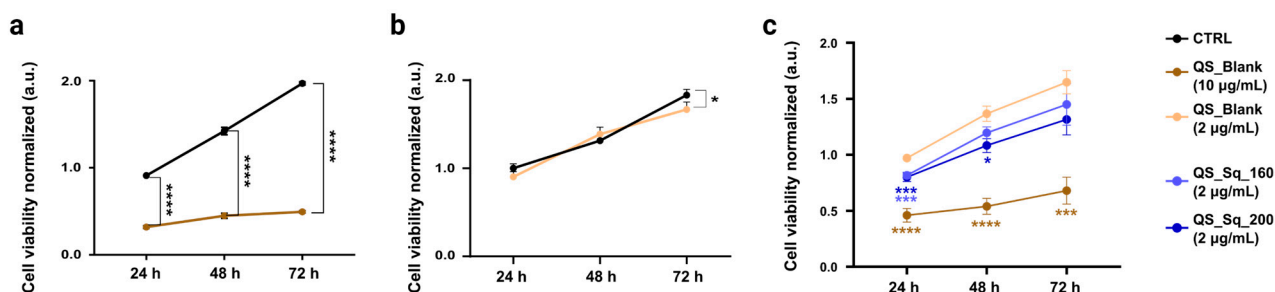


Figure 6. Cell viability assays based on a colorimetric method (MTT assay, $\text{Abs}_{490\text{nm}}$) on MCF-7 cells. Cells were treated O/N with QS_blank at two different concentrations of membrane components (Chol + Stk): 10 $\mu\text{g}/\text{mL}$ (a) and 2 $\mu\text{g}/\text{mL}$ (b). Data refer to one experiment representative of three. Statistical significance versus CNTRL (MCF-7 untreated): * $p < 0.05$, *** $p < 0.0001$ (t -test or Mann–Whitney test). (c) Cell viability assays on MCF-7 O/N treated with 10 $\mu\text{g}/\text{mL}$ (brown line) and 2 $\mu\text{g}/\text{mL}$ (beige line) of QS_blank, and 2 $\mu\text{g}/\text{mL}$ QS loaded with 160 and 200 μM of **Br-Sq-C12** (light blue and blue lines, respectively). Data are normalized on CNTRL at 24 h and represented as mean \pm SEM of three independent experiments. Statistical significance versus 2 $\mu\text{g}/\text{mL}$ QS blank: *** $p < 0.001$, **** $p < 0.0001$ (Ordinary one-way ANOVA with post-hoc Dunnett's multiple comparisons test).

The photoactivity of the molecules was quantified by irradiating MCF-7 cells for 15 min in the presence of free **Br-Sq-C12** or **Br-Sq-C12** incorporated into the previously described QS nanosystem (Figure 7). Interestingly, Sq-loaded QS are significantly more phototoxic than free Sq, even at the lowest concentration tested. In fact, **Br-Sq-C12**, in its free form, showed no phototoxicity at any of the tested concentrations (data shown in Figure S6). Of all formulations, QS_Sq_160 (at a final **Br-Sq-C12** concentration of 68 nM) was found to be the most active formulation, as it was significantly different from free **Br-**

Sq-C12 at all monitored time points (Figure 7). On the contrary, **QS_Sq_200** (corresponding to 85 nM effective dye concentration) did not yield a significant improvement in the photoactive properties of the nanosystem after irradiation. Those results point out that a higher concentration of photosensitizer in nanovesicles does not always correlate to higher PDT efficiency. We suspect that **Br-Sq-C12** molecules in the **QS_Sq_200** suffer from aggregation due to the higher concentration compared to **QS_Sq_160**, leading to a decrease of the squaraine photochemical properties and, in consequence, a lower PDT efficiency.

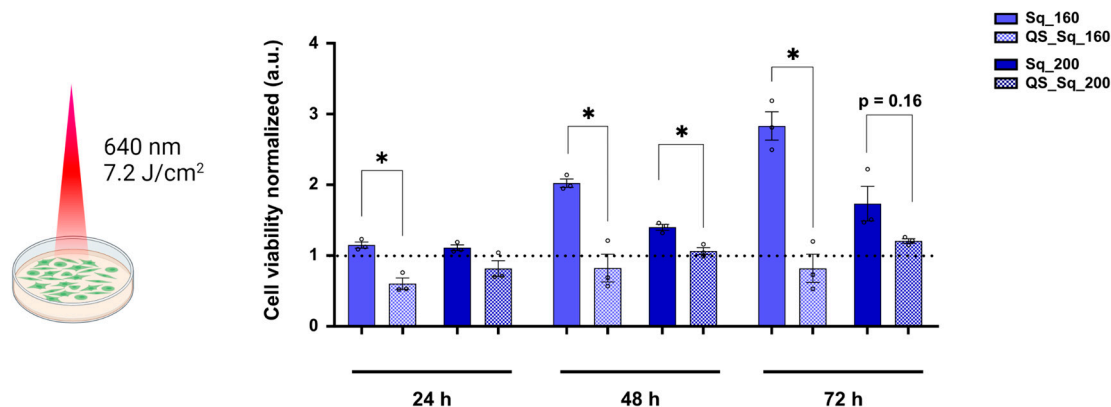


Figure 7. PDT evaluation on MCF-7 O/N treated with **Br-Sq-C12** in its free form or incorporated into QS (2 $\mu\text{g}/\text{mL}$) at 24, 48, and 72 h after LED irradiation (640 nm, 7.2 J/cm^2). Data are normalized on their own CNTRL (Br-Sq-12 samples on irradiated cells not treated; QS_Sq samples on irradiated cells treated with blank QS) at 24 h (dot line) and represented as mean \pm SEM of three independent experiments. Statistical significance between Sq and QS_Sq: * $p < 0.05$ (paired t -test or Wilcoxon test).

Of note, the concentration of free squaraine usually employed for PDT studies ranges from 1 to 100 μM [49,67,68]. Here, we show that the use of a nanocarrier system allows using much lower concentrations of photosensitizer (up to 10–1000 times lower). In agreement with previous data obtained on other types of nanosystems [24], our results demonstrate that the encapsulation within QS highly enhances the dye's photoactivity. It is likely that the nanocarrier, by significantly increasing the local concentration of the dye, in addition to reducing its aggregation phenomena, improves its overall spectroscopic properties. Furthermore, taking into account our results on ROS production (Figure 5), it is also possible to hypothesize that the relatively low photoactivity of the free dye in contact with MCF-7 cells may be due to a failure of the molecule to enter the cell, contrary to the nanoparticle system. To test this hypothesis, we performed confocal laser scan microscopy experiments on MCF-7 cells treated O/N with **QS_Sq_200** and the corresponding amount of **Br-Sq-C12** in its free form (85 nM). More specifically, we labeled the whole cellular volume using Calcein (illustrated in red), and, **Br-Sq-C12** is shown in blue (Figure 8). We acquired the images in three-dimensional space (XYZ), allowing the 3D cellular volume reconstruction and elucidating whether the **Br-Sq-C12** (encapsulated or in its free form) was included within the cellular volume. As shown in Figure 8a, we found that Sq-loaded QS are efficiently internalized by MCF-7 after O/N incubation as demonstrated by the orthogonal view, revealing probe signals included within the Calcein-labeled cell volume (orthogonal view in Figure 8a). By contrast, as previously hypothesized, the **Br-Sq-C12** in its free form at the same concentration present in the **Br-Sq-C12**-loaded QS samples was not properly internalized (Figure 8b). This confirms the absence of photoactivity due to hindered cellular uptake of the dye in its free form.

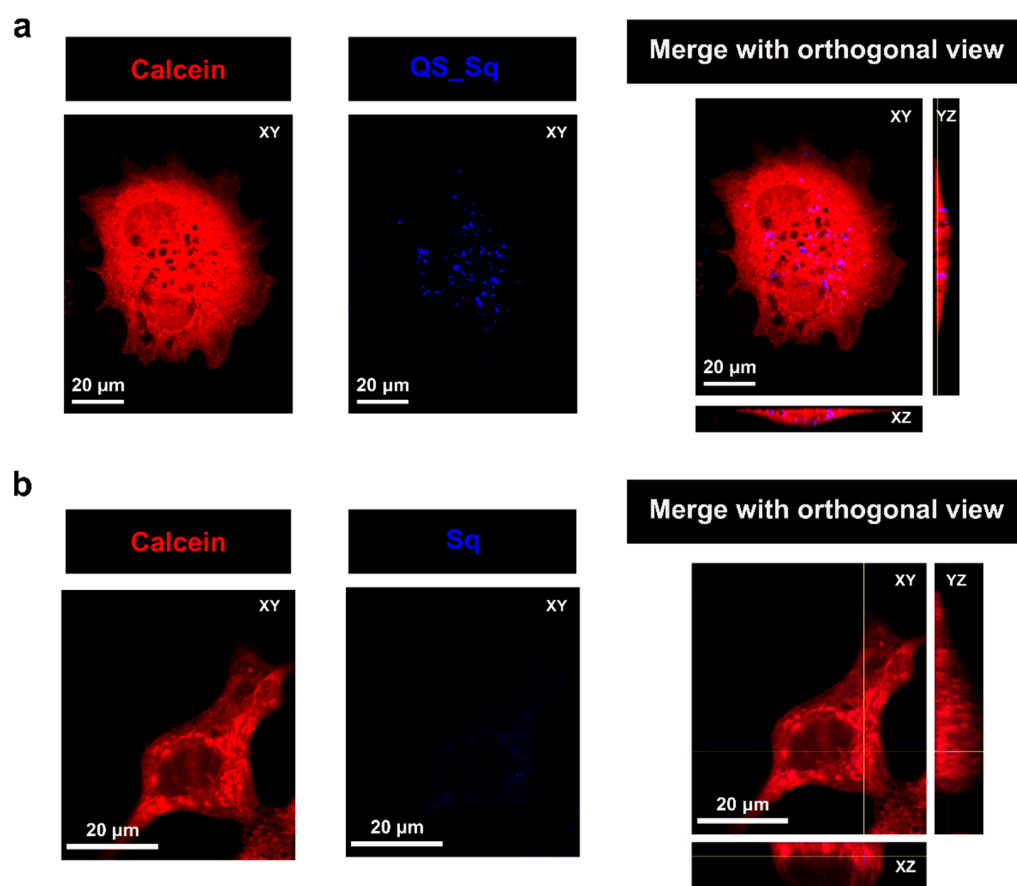


Figure 8. Representative confocal fluorescence images of MCF-7 cells incubated O/N with either QS_Sq_200 (QS_Sq) (a) or free Br-Sq-C12 (Sq) (b) at the same final concentration (85 nM). Red signals refer to Calcein ($\lambda_{ex}=561$ nm), and blue signals refer to squaraine ($\lambda_{ex}=633$ nm). For each sample, the overlay between the two signals in a 3D cellular volume reconstruction with orthogonal views is reported. Scale bar: 20 μ m.

Taken together, these results point out the advantage that nanoencapsulation supposes for photosensitizers such as squaraines. First, the entrapment of Br-Sq-C12 into a nanovesicular system such as QS allows not only its dispersity and stability in aqueous media but also the protection of its photophysical characteristics. Secondly, cell permeability issues that the PS faces in its free form can be overcome by its encapsulation (i.e., QS uptake through phagocytosis [42]). As a result, higher phototoxicity is observed for **Br-Sq-C12**-loaded QS than for the free dye.

4. Conclusions

A novel formulation based on Cholesterol–Sterealkonium QS loaded with a squaraine dye (i.e., Br-Sq-C12) has been proposed as an alternative photosensitizer in PDT. QS were prepared with green and scalable technology in a single step; the membrane components are available at pharmaceutical grade and readily adaptable for the incorporation of active targeting ligands. Considering the poor water solubility of squaraine dyes, their loading into QS offers an interesting strategy to bring them into aqueous media, enabling their use for bioapplications. Br-Sq-C12-loaded QS are stable for at least 18 weeks in aqueous media, showing modest dye leaking over time and weak photo instability. Moreover, we have demonstrated that Br-Sq-C12 incorporation into QS does not compromise its photophysical characteristics nor the ability of the dye to generate ROS rapidly, an essential requirement for PDT activity. Indeed, both the free Br-Sq-C12 and Br-Sq-C12-loaded QS possess faster and higher ROS generation ability compared to the well-known ROS generator Rose Bengal. Phototoxicity assays demonstrated that MCF-7 cells internalize

Br-Sq-C12-loaded QS, and upon irradiation, an increase in the apoptotic/necrotic cell population is observed. The higher phototoxicity observed for the QS-loaded Br-Sq-C12 vs. its free form can be explained by the higher efficiency in PS delivery. QS provides more photostability in the aqueous media, higher cellular uptake, and significantly increases the local concentration of the PS. Indeed, the use of the nanocarrier system allows using much lower concentrations of photoactive dye (up to 10–1000 times lower). Taken together, our in vitro results support the applicability of QS as nanocarriers for PDT application and highlight the benefits of encapsulating squaraine dyes into stable nanostructures to optimize their photoactive properties.

Supplementary Materials: The following Supporting Information can be downloaded at: <https://www.mdpi.com/article/10.3390/pharmaceutics15030902/s1>, Figure S1: Preliminary data with Br-Sq-C4; Figure S2: ¹H NMR spectrum of Br-Sq-C12; Figure S3: ESI-MS spectrum of Br-Sq-C12; Figure S4: QS stability after 18 months; Figure S5: Maximum absorbance peak over time of Br-Sq-C12-loaded QS; Figure S6: Cell viability assays with different concentrations of Br-Sq-12. Detailed protocol for the preparation of dye-loaded Chol/Stk QS by Delos-susp, including Table S1 with the initial reagents. DLS systematic study, including Figure S7: Absorption of Br-Sq-12 in comparison to DLS laser; Figure S8: Hydrodynamic diameter and PDI variation related to dilution; Figure S9: Comparison at two dilutions. Refs. [69,70] are cited in Supplementary Materials.

Author Contributions: Conceptualization, N.B. (Nadia Barbero), N.V. and M.K.; methodology, N.B. (Nicolò Bordignon), G.C., C.P. and E.S.; validation, G.V.-N., M.J.M.P. and J.M.-F.; formal analysis, A.F.P. and N.B. (Nicolò Bordignon); investigation, N.B. (Nicolò Bordignon), M.K., A.F.P., N.V. and N.B. (Nadia Barbero); data curation, J.M.-F., N.B. (Nadia Barbero) and M.K.; writing—original draft preparation, N.B. (Nicolò Bordignon) and J.M.-F.; writing—review and editing, M.K., N.V., J.M.-F. and N.B. (Nadia Barbero); supervision and project administration, M.K. and J.M.-F.; funding acquisition, N.V. and N.B. (Nadia Barbero). All authors have read and agreed to the published version of the manuscript.

Funding: J.M.-F. and M.K. gratefully thank the financial support received by the European Union's Horizon 2020 research and innovation program under the Marie Skłodowska-Curie grant agreement No. 712949 (TECNIOspring PLUS) and from the Agency for Business Competitiveness of the Government of Catalonia. This research was funded by the University of Torino, Ricerca Locale ex-60%, Linea A, Bando 2021, and, by the Fondazione CRT, II tornata 2019 RF.2019.2260. ICMAB-CSIC members acknowledge support from the Spanish Ministry of Science and Innovation (MICINN) for funding through the MOL4BIO project (No. PID2019-105622RB-I00), and the Spanish Ministry of Economic Affairs and Digital Transformation (MINECO) through the Severo Ochoa Program for Centers of Excellence in R&D (SEV-2015-0496 and CEX2019-000917-S), and the State Program for R&D&i (2016) orientated to the Society Challenges, modality RETOS-Collaboration 2016, and co-financed by FEDER funds from the European Commission (No. RTC-2016-4567-1, Nano4Derm). We also thank the financial support received by the European Union by EU Project MSCA-RISE-2020 RISE Action, 2021-2024 (No. 101007804, Micro4Nano). Furthermore, we would like to acknowledge funding from the Agaur agency of Generalitat de Catalunya through grant No. 2017-SGR-918 and 2021-SGR-00438. Quatsome production and their physicochemical characterization have been carried out at the Networking Research Centre on Bioengineering, Biomaterials, and Nanomedicine (CIBERBBN), financed by the Instituto de Salud Carlos III (ISCIII) with assistance from the European Regional Development Fund (ERDF). Biomaterial Processing and Nanostructuring Unit (U6) of the ICTS "NANBIOSIS," a unit of the CIBER network in Bioengineering, Biomaterials & Nanomedicine (CIBER-BBN) located at the Institute of Materials Science of Barcelona (ICMAB-CSIC).

Institutional Review Board Statement: Not applicable.

Informed Consent Statement: Not applicable.

Data Availability Statement: Not applicable.

Acknowledgments: We would like to acknowledge the preliminary work carried out by Primiano Pio Di Mauro, Nathaly Segovia, and Albert Revuelta for the development of Cholesterol–Sterealkonium QS in the frame of the project Nano4Derm (RTC-2016-4567-1), and by Lara Benoldi for the loading of Bromo-Squaraine-C4 (Br-Sq-C4) into quatsomes. The authors thank C. Medana (University of Torino) for the ESI-MS analysis.

Conflicts of Interest: The authors declare no conflict of interest. The funders had no role in the design of the study; in the collection, analyses, or interpretation of data; in the writing of the manuscript; or in the decision to publish the result.

References

1. Choi, Y.M.; Adelzadeh, L.; Wu, J.J. Photodynamic Therapy for Psoriasis. *J. Dermatol. Treat.* **2015**, *26*, 202–207. [[CrossRef](#)] [[PubMed](#)]
2. Makuch, S.; Drózd, M.; Makarec, A.; Ziółkowski, P.; Woźniak, M. An Update on Photodynamic Therapy of Psoriasis—Current Strategies and Nanotechnology as a Future Perspective. *Int. J. Mol. Sci.* **2022**, *23*, 9845. [[CrossRef](#)]
3. Xu, H.-Z.; Li, T.-F.; Ma, Y.; Li, K.; Zhang, Q.; Xu, Y.-H.; Zhang, Y.-C.; Zhao, L.; Chen, X. Targeted Photodynamic Therapy of Glioblastoma Mediated by Platelets with Photo-Controlled Release Property. *Biomaterials* **2022**, *290*, 121833. [[CrossRef](#)]
4. Akasov, R.A.; Sholina, N.V.; Khochenkov, D.A.; Alova, A.V.; Gorelkin, P.V.; Erofeev, A.S.; Generalova, A.N.; Khaydukov, E.V. Photodynamic Therapy of Melanoma by Blue-Light Photoactivation of Flavin Mononucleotide. *Sci. Rep.* **2019**, *9*, 9679. [[CrossRef](#)] [[PubMed](#)]
5. Dolmans, D.E.J.G.J.; Fukumura, D.; Jain, R.K. Photodynamic Therapy for Cancer. *Nat. Rev. Cancer* **2003**, *3*, 380–387. [[CrossRef](#)] [[PubMed](#)]
6. Gunaydin, G.; Gedik, M.E.; Ayan, S. Photodynamic Therapy—Current Limitations and Novel Approaches. *Front. Chem.* **2021**, *9*, 691697. [[CrossRef](#)]
7. McDonald, I.A.N.J.; Dougherty, T.J. Basic Principles of Photodynamic Therapy. *J. Porphyr. Phthalocyanines* **2001**, *05*, 105–129. [[CrossRef](#)]
8. Henderson, B.W.; Dougherty, T.J. How does Photodynamic therapy work? *Photochem. Photobiol.* **1992**, *55*, 145–157. [[CrossRef](#)]
9. Kwiatkowski, S.; Knap, B.; Przystupski, D.; Saczko, J.; Kędzierska, E.; Knap-Czop, K.; Kotlińska, J.; Michel, O.; Kotowski, K.; Kulbacka, J. Photodynamic Therapy—Mechanisms, Photosensitizers and Combinations. *Biomed. Pharmacother.* **2018**, *106*, 1098–1107. [[CrossRef](#)] [[PubMed](#)]
10. Falk-Mahapatra, R.; Gollnick, S.O. Photodynamic Therapy and Immunity: An Update. *Photochem. Photobiol.* **2020**, *96*, 550–559. [[CrossRef](#)]
11. Allison, R.R.; Downie, G.H.; Cuenca, R.; Hu, X.-H.; Childs, C.J.H.; Sibata, C.H. Photosensitizers in Clinical PDT. *Photodiagn. Photodyn.* **2004**, *1*, 27–42. [[CrossRef](#)] [[PubMed](#)]
12. O'Connor, A.E.; Gallagher, W.M.; Byrne, A.T. Porphyrin and Nonporphyrin Photosensitizers in Oncology: Preclinical and Clinical Advances in Photodynamic Therapy. *Photochem. Photobiol.* **2009**, *85*, 1053–1074. [[CrossRef](#)]
13. Baskaran, R.; Lee, J.; Yang, S.-G. Clinical Development of Photodynamic Agents and Therapeutic Applications. *Biomater. Res.* **2018**, *22*, 25. [[CrossRef](#)]
14. Berlanda, J.; Kiesslich, T.; Engelhardt, V.; Krammer, B.; Plaetzer, K. Comparative in Vitro Study on the Characteristics of Different Photosensitizers Employed in PDT. *J. Photochem. Photobiol. B* **2010**, *100*, 173–180. [[CrossRef](#)] [[PubMed](#)]
15. Reynolds, T. Photodynamic Therapy Expands Its Horizons. *JNCI J. Natl. Cancer Inst.* **1997**, *89*, 112–114. [[CrossRef](#)]
16. Wyss, P.; Schwarz, V.; Dobler-Girdziunaite, D.; Hornung, R.; Walt, H.; Degen, A.; Fehr, M. Photodynamic Therapy of Locoregional Breast Cancer Recurrences Using a Chlorin-Type Photosensitizer. *Int. J. Cancer* **2001**, *93*, 720–724. [[CrossRef](#)]
17. Bown, S.G.; Rogowska, A.Z.; Whitelaw, D.E.; Lees, W.R.; Lovat, L.B.; Ripley, P.; Jones, L.; Wyld, P.; Gillams, A.; Hatfield, A.W.R. Photodynamic Therapy for Cancer of the Pancreas. *Gut* **2002**, *50*, 549. [[CrossRef](#)] [[PubMed](#)]
18. Dereje, D.M.; Pontremoli, C.; Moran Plata, M.J.; Visentin, S.; Barbero, N. Polymethine Dyes for PDT: Recent Advances and Perspectives to Drive Future Applications. *Photochem. Photobiol. Sci.* **2022**, *21*, 397–419. [[CrossRef](#)] [[PubMed](#)]
19. Avirah, R.R.; Jayaram, D.T.; Adarsh, N.; Ramaiah, D. Squaraine Dyes in PDT: From Basic Design to in Vivo Demonstration. *Org. Biomol. Chem.* **2012**, *10*, 911–920. [[CrossRef](#)] [[PubMed](#)]
20. D'Alessandro, S.; Priefer, R. Non-Porphyrin Dyes Used as Photosensitizers in Photodynamic Therapy. *J. Drug Deliv. Sci. Technol.* **2020**, *60*, 101979. [[CrossRef](#)]
21. Lange, N.; Szlasa, W.; Saczko, J.; Chwiłkowska, A. Potential of Cyanine Derived Dyes in Photodynamic Therapy. *Pharmaceutics* **2021**, *13*, 818. [[CrossRef](#)]
22. Pontremoli, C.; Chinigò, G.; Galliano, S.; Moran Plata, M.J.; Dereje, D.M.; Sansone, E.; Gilardino, A.; Barolo, C.; Fiorio Pla, A.; Visentin, S.; et al. Photosensitizers for Photodynamic Therapy: Structure-Activity Analysis of Cyanine Dyes through Design of Experiments. *Dye. Pigment.* **2023**, *210*, 111047. [[CrossRef](#)]
23. Iliina, K.; MacCuaig, W.M.; Laramie, M.; Jeouty, J.N.; McNally, L.R.; Henary, M. Squaraine Dyes: Molecular Design for Different Applications and Remaining Challenges. *Bioconjugate Chem.* **2020**, *31*, 194–213. [[CrossRef](#)] [[PubMed](#)]

24. Chinigò, G.; Gonzalez-Paredes, A.; Gilardino, A.; Barbero, N.; Barolo, C.; Gasco, P.; Fiorio Pla, A.; Visentin, S. Polymethine Dyes-Loaded Solid Lipid Nanoparticles (SLN) as Promising Photosensitizers for Biomedical Applications. *Spectrochim. Acta A Mol. Biomol. Spectrosc.* **2022**, *271*, 120909. [[CrossRef](#)] [[PubMed](#)]
25. Escudero, A.; Carrillo-Carrión, C.; Castillejos, M.C.; Romero-Ben, E.; Rosales-Barrios, C.; Khiar, N. Photodynamic Therapy: Photosensitizers and Nanostructures. *Mater. Chem. Front.* **2021**, *5*, 3788–3812. [[CrossRef](#)]
26. Miletto, I.; Fraccarollo, A.; Barbero, N.; Barolo, C.; Cossi, M.; Marchese, L.; Gianotti, E. Mesoporous Silica Nanoparticles Incorporating Squaraine-Based Photosensitizers: A Combined Experimental and Computational Approach. *Dalton Trans.* **2018**, *47*, 3038–3046. [[CrossRef](#)] [[PubMed](#)]
27. Vargas-Nadal, G.; Köber, M.; Nsamela, A.; Terenziani, F.; Sissa, C.; Pescina, S.; Sonvico, F.; Gazzali, A.M.; Wahab, H.A.; Grisanti, L.; et al. Fluorescent Multifunctional Organic Nanoparticles for Drug Delivery and Bioimaging: A Tutorial Review. *Pharmaceutics* **2022**, *14*, 2498. [[CrossRef](#)]
28. Jia, H.-R.; Zhu, Y.-X.; Xu, K.-F.; Liu, X.; Wu, F.-G. Plasma Membrane-Anchorable Photosensitizing Nanomicelles for Lipid Raft-Responsive and Light-Controllable Intracellular Drug Delivery. *J. Control. Release* **2018**, *286*, 103–113. [[CrossRef](#)]
29. Yang, Y.; Wang, L.; Cao, H.; Li, Q.; Li, Y.; Han, M.; Wang, H.; Li, J. Photodynamic Therapy with Liposomes Encapsulating Photosensitizers with Aggregation-Induced Emission. *Nano Lett.* **2019**, *19*, 1821–1826. [[CrossRef](#)]
30. Dong, S.; Teo, J.D.W.; Chan, L.Y.; Lee, C.-L.K.; Sou, K. Far-Red Fluorescent Liposomes for Folate Receptor-Targeted Bioimaging. *ACS Appl. Nano Mater.* **2018**, *1*, 1009–1013. [[CrossRef](#)]
31. Sun, Y.; Geng, X.; Wang, Y.; Su, X.; Han, R.; Wang, J.; Li, X.; Wang, P.; Zhang, K.; Wang, X. Highly Efficient Water-Soluble Photosensitizer Based on Chlorin: Synthesis, Characterization, and Evaluation for Photodynamic Therapy. *ACS Pharm. Transl. Sci.* **2021**, *4*, 802–812. [[CrossRef](#)] [[PubMed](#)]
32. Drogat, N.; Gady, C.; Granet, R.; Sol, V. Design and Synthesis of Water-Soluble Polyaminated Chlorins and Bacteriochlorins—With near-Infrared Absorption. *Dye. Pigment.* **2013**, *98*, 609–614. [[CrossRef](#)]
33. Han, J.; Park, W.; Park, S.; Na, K. Photosensitizer-Conjugated Hyaluronic Acid-Shielded Polydopamine Nanoparticles for Targeted Photomediated Tumor Therapy. *ACS Appl. Mater. Interfaces* **2016**, *8*, 7739–7747. [[CrossRef](#)]
34. Sheng, Z.; Hu, D.; Zheng, M.; Zhao, P.; Liu, H.; Gao, D.; Gong, P.; Gao, G.; Zhang, P.; Ma, Y.; et al. Smart Human Serum Albumin-Indocyanine Green Nanoparticles Generated by Programmed Assembly for Dual-Modal Imaging-Guided Cancer Synergistic Phototherapy. *ACS Nano* **2014**, *8*, 12310–12322. [[CrossRef](#)] [[PubMed](#)]
35. Son, J.; Yang, S.M.; Yi, G.; Roh, Y.J.; Park, H.; Park, J.M.; Choi, M.-G.; Koo, H. Folate-Modified PLGA Nanoparticles for Tumor-Targeted Delivery of Pheophorbide a in Vivo. *Biochem. Biophys. Res. Commun.* **2018**, *498*, 523–528. [[CrossRef](#)] [[PubMed](#)]
36. Maeda, H.; Wu, J.; Sawa, T.; Matsumura, Y.; Hori, K. Tumor Vascular Permeability and the EPR Effect in Macromolecular Therapeutics: A Review. *J. Control. Release* **2000**, *65*, 271–284. [[CrossRef](#)]
37. Sharma, A.; Sharma, U.S. Liposomes in Drug Delivery: Progress and Limitations. *Int. J. Pharm.* **1997**, *154*, 123–140. [[CrossRef](#)]
38. Sercombe, L.; Veerati, T.; Moheimani, F.; Wu, S.Y.; Sood, A.K.; Hua, S. Advances and Challenges of Liposome Assisted Drug Delivery. *Front. Pharm.* **2015**, *6*, 286. [[CrossRef](#)]
39. Lee, E.-H.; Lim, S.-J.; Lee, M.-K. Chitosan-Coated Liposomes to Stabilize and Enhance Transdermal Delivery of Indocyanine Green for Photodynamic Therapy of Melanoma. *Carbohydr. Polym.* **2019**, *224*, 115143. [[CrossRef](#)]
40. Köber, M.; Illa-Tuset, S.; Ferrer-Tasies, L.; Moreno-Calvo, E.; Tatkiewicz, W.I.; Grimaldi, N.; Piña, D.; Pérez, A.P.; Lloveras, V.; Vidal-Gancedo, J.; et al. Stable Nanovesicles Formed by Intrinsically Planar Bilayers. *J. Colloid Interface Sci.* **2023**, *631*, 202–211. [[CrossRef](#)]
41. Ferrer-Tasies, L.; Moreno-Calvo, E.; Cano-Sarabia, M.; Aguilera-Arzo, M.; Angelova, A.; Lesieur, S.; Ricart, S.; Faraudo, J.; Ventosa, N.; Veciana, J. Quatsomes: Vesicles Formed by Self-Assembly of Sterols and Quaternary Ammonium Surfactants. *Langmuir* **2013**, *29*, 6519–6528. [[CrossRef](#)] [[PubMed](#)]
42. Morla-Folch, J.; Vargas-Nadal, G.; Zhao, T.; Sissa, C.; Ardizzzone, A.; Kurhuzenkau, S.; Köber, M.; Uddin, M.; Painelli, A.; Veciana, J.; et al. Dye-Loaded Quatsomes Exhibiting FRET as Nanoprobes for Bioimaging. *ACS Appl. Mater. Interfaces* **2020**, *12*, 20253–20262. [[CrossRef](#)] [[PubMed](#)]
43. Vargas-Nadal, G.; Muñoz-Ubeda, M.; Alamo, P.; Arnal, M.M.; Céspedes, V.; Köber, M.; Gonzalez, E.; Ferrer-Tasies, L.; Vinardell, M.P.; Mangues, R.; et al. MKC-Quatsomes: A Stable Nanovesicle Platform for Bio-Imaging and Drug-Delivery Applications. *Nanomedicine* **2020**, *24*, 102136. [[CrossRef](#)]
44. Kou, L.; Bhutia, Y.D.; Yao, Q.; He, Z.; Sun, J.; Ganapathy, V. Transporter-Guided Delivery of Nanoparticles to Improve Drug Permeation across Cellular Barriers and Drug Exposure to Selective Cell Types. *Front. Pharm.* **2018**, *9*, 27. [[CrossRef](#)] [[PubMed](#)]
45. Blanco, E.; Shen, H.; Ferrari, M. Principles of Nanoparticle Design for Overcoming Biological Barriers to Drug Delivery. *Nat. Biotechnol.* **2015**, *33*, 941–951. [[CrossRef](#)]
46. Andreas, R.; Klymchenko, A.S. Fluorescent Polymer Nanoparticles Based on Dyes: Seeking Brighter Tools for Bioimaging. *Small* **2016**, *12*, 1968–1992. [[CrossRef](#)]
47. Cabrera, I.; Elizondo, E.; Esteban, O.; Corchero, J.L.; Melgarejo, M.; Pulido, D.; Córdoba, A.; Moreno, E.; Unzueta, U.; Vazquez, E.; et al. Multifunctional Nanovesicle-Bioactive Conjugates Prepared by a One-Step Scalable Method Using CO₂-Expanded Solvents. *Nano Lett.* **2013**, *13*, 3766–3774. [[CrossRef](#)]

48. Martínez-Miguel, M.; Castellote-Borrell, M.; Köber, M.; Kyvik, A.R.; Tomsen-Melero, J.; Vargas-Nadal, G.; Muñoz, J.; Pulido, D.; Cristóbal-Lecina, E.; Passemard, S.; et al. Hierarchical Quatsome-RGD Nanoarchitectonic Surfaces for Enhanced Integrin-Mediated Cell Adhesion. *ACS Appl. Mater. Interfaces* **2022**, *14*, 48179–48193. [[CrossRef](#)]
49. Serpe, L.; Ellena, S.; Barbero, N.; Foglietta, F.; Prandini, F.; Gallo, M.P.; Levi, R.; Barolo, C.; Canaparo, R.; Visentin, S. Squaraines Bearing Halogenated Moieties as Anticancer Photosensitizers: Synthesis, Characterization and Biological Evaluation. *Eur. J. Med. Chem.* **2016**, *113*, 187–197. [[CrossRef](#)]
50. Barbero, N.; Magistris, C.; Park, J.; Saccone, D.; Quagliotto, P.; Buscaino, R.; Medana, C.; Barolo, C.; Viscardi, G. Microwave-Assisted Synthesis of Near-Infrared Fluorescent Indole-Based Squaraines. *Org. Lett.* **2015**, *17*, 3306–3309. [[CrossRef](#)]
51. Ventosa, N.; Veciana, J.; Sala, S.; Cano, M. Method for Obtaining Micro- and Nano-Disperse Systems. WO 2006/079889, 3 August 2006.
52. Vargas-Nadal, G.; Ventosa, N.; Ferrer-Tasies, L. *Novel Quatsome Nanovesicles, Prepared Using CO₂, for the Development of Advanced Nanomedicines*; Universitat de Barcelona: Barcelona, Spain, 2020.
53. Delgado, A.v.; González-Caballero, F.; Hunter, R.J.; Koopal, L.K.; Lyklema, J. Measurement and Interpretation of Electrokinetic Phenomena (IUPAC Technical Report). *Pure Appl. Chem.* **2005**, *77*, 1753–1805. [[CrossRef](#)]
54. Ardizzzone, A.; Veciana i Miró, J.; Ventosa, N.; Pleixats i Rovira, R. *New Fluorescent Nanovesicles, by Self-Assembly of Organic Fluorophores, Sterols and Surfactants, as Probes for Bioimaging*; Departament de Química, Universitat Autònoma de Barcelona: Barcelona, Spain, 2017.
55. Ardizzzone, A.; Kurhuzenkau, S.; Illa-Tuset, S.; Faraudo, J.; Bondar, M.; Hagan, D.; van Stryland, E.W.; Painelli, A.; Sissa, C.; Feiner, N.; et al. Nanostructuring Lipophilic Dyes in Water Using Stable Vesicles, Quatsomes, as Scaffolds and Their Use as Probes for Bioimaging. *Small* **2018**, *14*, 1703851. [[CrossRef](#)]
56. Morla-Folch, J.; Vargas-Nadal, G.; Fuentes, E.; Illa-Tuset, S.; Köber, M.; Sissa, C.; Pujals, S.; Painelli, A.; Veciana, J.; Faraudo, J.; et al. Ultrabright Förster Resonance Energy Transfer Nanovesicles: The Role of Dye Diffusion. *Chem. Mater.* **2022**, *34*, 8517–8527. [[CrossRef](#)]
57. Liu, X.; Ardizzzone, A.; Sui, B.; Anzola, M.; Ventosa, N.; Liu, T.; Veciana, J.; Belfield, K.D. Fluorenyl-Loaded Quatsome Nanostructured Fluorescent Probes. *ACS Omega* **2017**, *2*, 4112–4122. [[CrossRef](#)] [[PubMed](#)]
58. Samimi, S.; Maghsoudnia, N.; Eftekhari, R.B.; Dorkoosh, F. Chapter 3—Lipid-Based Nanoparticles for Drug Delivery Systems. In *Micro and Nano Technologies*; Mohapatra, S., Ranjan, S., Dasgupta, N., Mishra, R., Thomas, S., Eds.; Elsevier: Amsterdam, The Netherlands, 2019; pp. 47–76. ISBN 978-0-12-814031-4.
59. Alberto, G.; Barbero, N.; Divieto, C.; Rebba, E.; Sassi, M.P.; Viscardi, G.; Martra, G. Solid Silica Nanoparticles as Carriers of Fluorescent Squaraine Dyes in Aqueous Media: Toward a Molecular Engineering Approach. *Colloids Surf. A Phys. Eng. Asp.* **2019**, *568*, 123–130. [[CrossRef](#)]
60. Park, J.; Barbero, N.; Yoon, J.; Dell’Orto, E.; Galliano, S.; Borrelli, R.; Yum, J.-H.; di Censo, D.; Grätzel, M.; Nazeeruddin, M.K.; et al. Panchromatic Symmetrical Squaraines: A Step Forward in the Molecular Engineering of Low Cost Blue-Greenish Sensitizers for Dye-Sensitized Solar Cells. *Phys. Chem. Chem. Phys.* **2014**, *16*, 24173–24177. [[CrossRef](#)]
61. Barbero, N.; Butnarusu, C.; Visentin, S.; Barolo, C. Squaraine Dyes: Interaction with Bovine Serum Albumin to Investigate Supramolecular Adducts with Aggregation-Induced Emission (AIE) Properties. *Chem. Asian J.* **2019**, *14*, 896–903. [[CrossRef](#)]
62. Ciubini, B.; Visentin, S.; Serpe, L.; Canaparo, R.; Fin, A.; Barbero, N. Design and Synthesis of Symmetrical Pentamethine Cyanine Dyes as NIR Photosensitizers for PDT. *Dye. Pigment.* **2019**, *160*, 806–813. [[CrossRef](#)]
63. Galliano, S.; Novelli, V.; Barbero, N.; Smarra, A.; Viscardi, G.; Borrelli, R.; Sauvage, F.; Barolo, C. Dicyanovinyl and Cyano-Ester Benzoindolenine Squaraine Dyes: The Effect of the Central Functionalization on Dye-Sensitized Solar Cell Performance. *Energies* **2016**, *9*, 486. [[CrossRef](#)]
64. Magistris, C.; Martiniani, S.; Barbero, N.; Park, J.; Benzi, C.; Anderson, A.; Law, C.; Barolo, C.; O’Regan, B. Near-Infrared Absorbing Squaraine Dye with Extended π Conjugation for Dye-Sensitized Solar Cells. *Renew. Energy* **2013**, *60*, 672–678. [[CrossRef](#)]
65. Zhang, S.; Ding, S.; Yu, J.; Chen, X.; Lei, Q.; Fang, W. Antibacterial Activity, in Vitro Cytotoxicity, and Cell Cycle Arrest of Gemini Quaternary Ammonium Surfactants. *Langmuir* **2015**, *31*, 12161–12169. [[CrossRef](#)] [[PubMed](#)]
66. Elder, R.L. Final Report on the Safety Assessment of Stearalkonium Chloride. *J. Am. Coll. Toxicol.* **1982**, *1*, 57–69. [[CrossRef](#)]
67. Rapozzi, V.; Beverina, L.; Salice, P.; Pagani, G.A.; Camerin, M.; Xodo, L.E. Photooxidation and Phototoxicity of π -Extended Squaraines. *J. Med. Chem.* **2010**, *53*, 2188–2196. [[CrossRef](#)]
68. Shafeekh, K.M.; Soumya, M.S.; Rahim, M.A.; Abraham, A.; Das, S. Synthesis and Characterization of Near-Infrared Absorbing Water Soluble Squaraines and Study of Their Photodynamic Effects in DLA Live Cells. *Photochem. Photobiol.* **2014**, *90*, 585–595. [[CrossRef](#)] [[PubMed](#)]
69. Geißler, D.; Gollwitzer, C.; Sikora, A.; Minelli, C.; Krumrey, M.; Resch-Genger, U. Effect of Fluorescent Staining on Size Measurements of Polymeric Nanoparticles Using DLS and SAXS. *Anal. Methods* **2015**, *7*, 9785–9790. [[CrossRef](#)]
70. Elizondo, E.; Larsen, J.; Hatzakis, N.S.; Cabrera, I.; Bjørnholm, T.; Veciana, J.; Stamou, D.; Ventosa, N. Influence of the Preparation Route on the Supramolecular Organization of Lipids in a Vesicular System. *J. Am. Chem. Soc.* **2012**, *134*, 1918–1921. [[CrossRef](#)]

Disclaimer/Publisher’s Note: The statements, opinions and data contained in all publications are solely those of the individual author(s) and contributor(s) and not of MDPI and/or the editor(s). MDPI and/or the editor(s) disclaim responsibility for any injury to people or property resulting from any ideas, methods, instructions or products referred to in the content.